Bani Asadi, Hossein; Borandeh, Sedigheh; Seppälä, Jukka

High-Performance and Biobased Polyamide/Functionalized Graphene Oxide Nanocomposites through In Situ Polymerization for Engineering Applications

Published in:
Macromolecular Materials and Engineering

DOI:
10.1002/mame.202100255

Published: 01/10/2021

Document Version
Publisher's PDF, also known as Version of record

RESEARCH ARTICLE

Macromolecular Materials and Engineering

www.mame-journal.de

High-Performance and Biobased Polyamide/Functionalized Graphene Oxide Nanocomposites through In Situ Polymerization for Engineering Applications

*Hossein Baniasadi, Sedigheh Borandeh, and Jukka Seppälä**

In this study, biobased polyamide/functionalized graphene oxide (PA-FGO) nanocomposite is developed using sustainable resources. Renewable PA is synthesized via polycondensation of hexamethylenediamine (HMDA) and biobased tetradecanedioic acid. Furthermore, GO is functionalized with HMDA to improve its compatibility with biobased PA and in situ polymerization is employed to obtain homogeneous PA-FGO nanocomposites. Compatibility improvement provides simultaneous increases in the tensile strength, storage modulus, and conductivity of PA by adding only 2 wt% FGO (PA-FGO2). The tensile strength and storage modulus of PA-FGO2 nanocomposite are enhanced dramatically by ≈50% and 30%, respectively, and the electrical conductivity reached 3.80×10^{-3} S m^{-1}. In addition, rheology testing confirms a shear-thinning trend for all samples as well as a significant enhancement in the storage modulus upon increasing the FGO content due to a rigid network formation and strong polymer-filler interactions. All these improvements strongly support the excellent compatibility and enhanced interfacial interactions between organic–inorganic phases resulting from GO surface functionalization. It is expected that the biobased PA-FGO nanocomposites with remarkable thermomechanical properties developed here can be used to design high-performance structures for demanded engineering applications.

1. Introduction

Polyamide (PA), as one of the most widely used synthetic polymers, has been investigated for decades in different engineering fields, such as automotive parts, construction materials, and fibers. PA possesses excellent mechanical properties even at high temperatures, low gas permeability, and outstanding resistance to wear, abrasion, and chemicals.[1–3] However, due to serious environmental problems related to greenhouse gas emissions, global warming, and depletion of fossil resources, studies have focused on developing biobased PAs in which at least one monomer derives from renewable and sustainable resources. Biobased PAs are of great interest academically and industrially due to improving the carbon footprint of plastic products and positively impacting their life-cycle evaluation.[4–6] On the other hand, nanofillers have been used frequently for improving the mechanical, physical, and wear properties of biobased PAs and consequently obtain high-performance nanocomposites for engineering applications.[7–9] A small loading of nanofiller into a polymer matrix could result in nanocomposites with excellent stiffness, boosted mechanical strength, enhanced gas barrier property, and higher thermal stability. Among various nanofillers, graphene is one of the most promising owing to its high Young's modulus, carrier mobility, thermal and electrical conductivity, and specific surface area.[10–12] High-performance PA/graphene nanocomposite leads to user-friendly end products for a wide range of applications, including fuel cells, supercapacitors, energy devices, automobiles, electronics, solar cell, gas detection, functional conducting electrodes for technical use, lithium-ion batteries, and so on.[13]

Nevertheless, graphene tends to aggregate into the polymer matrix due to its high surface area and strong Van der Waals force interactions. The consequent dispersion and interfacial interactions of graphene with the polymer matrix can affect the satisfactory performance of the final nanocomposites.[14,15] Appropriate surface functionalization of graphene is therefore needed in order to develop strong interactions between PA and graphene. Surface functionalization of graphene with small-molecule compounds and grafting with polymer chains are two standard methods to achieve this.[14,16] Functionalized graphene has good dispersion stability in aqueous and organic solvents and can possess remarkable properties, including ultrahigh aspect ratio, good mechanical strength, high environmental and radiation stability,

H. Baniasadi, S. Borandeh, J. Seppälä
Polymer Technology
School of Chemical Engineering
Aalto University
Kemistintie 1, Espoo 02150, Finland
E-mail: jukka.seppala@aalto.fi

The ORCID identification number(s) for the author(s) of this article can be found under https://doi.org/10.1002/mame.202100255

DOI: 10.1002/mame.202100255

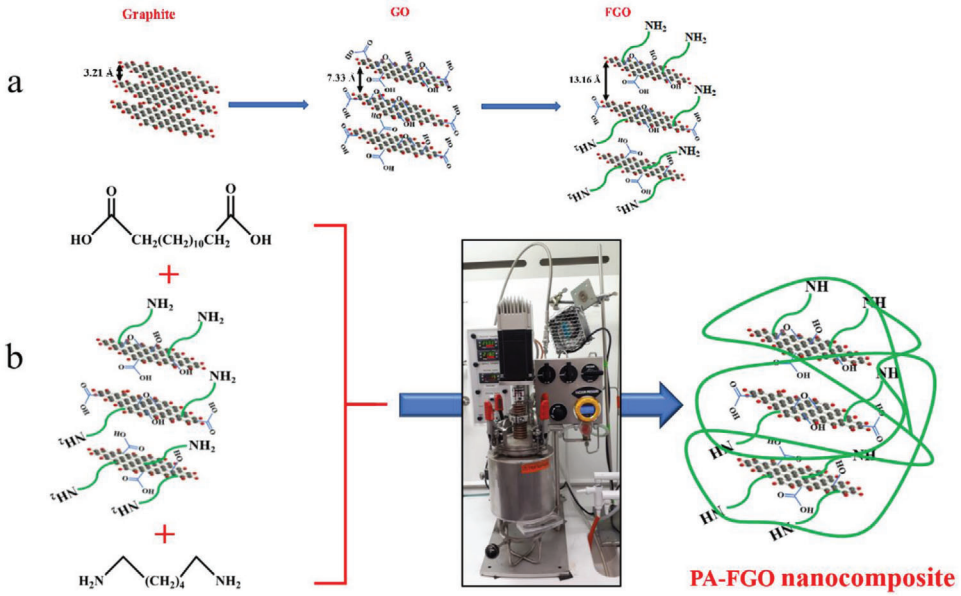

Figure 1. a) A schematic representation of GO functionalization with HMDA and b) preparation of PA-GO nanocomposite via in situ polymerization.

improved electrical conductivity, and superb barrier resistance against gases.[17–19] Accordingly, graphene oxide (GO), which is composed of oxygenated graphene layers and has increased interlayer spacing compared to pristine graphite, could be an appropriate candidate for further surface modification and, as a result, for improving the interaction and compatibility with the monomers and polymers.[11,12,20]

In order to improve the performance of PA nanocomposites and fulfill engineering demands, it is essential to gain a better insight into the correlations between polymer-nanofiller compatibility, property profiles, and nanocomposite fabrication methods. The main goal of this study is to develop a high-performance long-chain aliphatic biobased PA614/graphene nanocomposite with the aim of using functionalized GO (FGO) and in situ polymerization. The links between polymer-nanofiller compatibility, property profiles, and nanocomposite fabrication methods for improving the performance of PA nanocomposites to fulfill various engineering demands were thoroughly reviewed. Furthermore, the influence of different FGO content on the physical, mechanical, thermal, electrical, morphological, and rheological properties of the synthesized PA-FGO nanocomposites was investigated to introduce the optimum composition to fulfill the engineering applications requirements.

2. Results and Discussion

With the general aim of improving the thermal, mechanical, and physical properties of long-chain aliphatic biobased PAs for engineering applications, in this study, graphene nanosheets were used as reinforcements to obtain high-performance nanocomposites. Furthermore, in situ polymerization was performed on the surface of graphene layers so as to improve the compatibility between the PA matrix and graphene nanosheets and to obtain homogenous and high-performance PA/graphene nanocomposites with excellent interfacial interactions between graphene layers and polymer matrix. Accordingly, the surface of GO was functionalized using HMDA, through nucleophilic substitution reactions between $-NH_2$ groups in hexamethylenediamine (HMDA) and epoxy groups in the basal plane of GO, or through an amidation reaction with the carboxylic acids on GO edges. The free amine groups on the surface of FGO are expected to participate in polymerization with diacid during in situ polymerization and polymerization may occur between the graphene layers. A schematic representation of GO functionalization and the synthesis of PA-GO nanocomposite via in situ polymerization are provided in **Figure 1**.

2.1. FGO Characterization

2.1.1. Fourier Transform Infrared Spectroscopy (FT-IR) and Raman Spectroscopy

Graphite oxidation and functionalization were confirmed using FT-IR analysis. The spectra of graphite, GO, and FGO are shown in **Figure 2**a. The graphite FT-IR spectrum represented no prominent characteristic absorption bands, while GO showed a broad and strong absorption band at 3000–3680 cm^{-1}, confirming the presence of hydroxyl functionalities (–OH) at the basal plane of the graphitic structure. Furthermore, some other characteristic bands at 1715, 1616, and 1043 cm^{-1} were detected and these were attributed to the stretching vibrations of carbonyl groups of carboxylic acids C=O, C=C, and C–O–C groups, respectively. Together, these characteristic peaks confirmed that graphite was oxidized to GO and the graphite sheets containing rich oxygen functionalities at their basal plane and edges were prepared.[21] Unlike GO, the intensity of the peaks at 3000–3680 cm^{-1} (hydroxyl groups) and 1750 cm^{-1} (acidic C=O) decreased in the FGO spectrum owing to the attachment of HMDA onto the surface and edges of GO through a nucleophilic reaction between amine

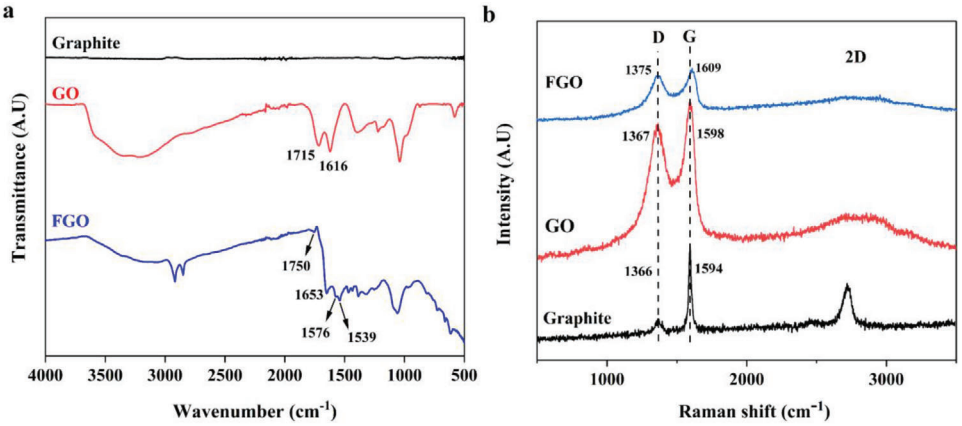

Figure 2. a) FT-IR and b) Raman spectra of graphite, GO, and FGO.

Table 1. The I_D/I_G ratio and crystalline size of graphite, GO, and FGO.

Sample	I_D/I_G	L_a [nm]
Graphite	0.35	12.43
GO	0.92	4.73
FGO	0.98	4.44

Table 2. Elemental analysis data of graphite, GO, and FGO.

Sample	C [wt%]	H [wt%]	N [wt%]	O [wt%]	S [wt%]	O/C [%]
Graphite	93.5	0.53	0	5.9	0	6.3
GO	52.5	2.2	0	44.6	0.7	84.9
FGO	62.3	5.7	8.2	23.3	0.5	37.4

groups of HMDA with epoxy groups of GO, and an amidation reaction with GO carboxylic acids. Some new peaks were also be detected at 2917–2850, 1653, 1576, and 1539 cm^{-1} and these were attributed to the aliphatic $-CH_2$ groups of HMDA, stretching vibrations of amide carbonyl (amidic C═O), C═C, and –NH groups, respectively. Overall, the FT-IR spectra confirmed that the nucleophilic substitution and amidation reactions took place, and, subsequently, amine and amide bonds were formed on the surface and edges of GO.

Raman spectroscopy was employed to investigate the structural changes in graphite after oxidation and functionalization with HMDA. Three characteristic peaks could be detected in the Raman spectra of graphite, GO, and FGO, including D, G, and 2D (Figure 2b). The G peak is related to the first-order scattering of the E_{2g} phonon of sp^2 carbon atoms, while the D peak is attributed to local sp^3 defects or disorder bands caused by oxidation and/or functionalization.[21,22] **Table 1** summarizes the intensity ratio of D and G bands (I_D/I_G). This was used to estimate the atomic ratio of sp^2/sp^3 carbon atoms and the amount of disorder in the graphene-based materials. The ratio of I_D/I_G rose from 0.35 in graphite to 0.92 in GO, confirming the oxygen functionalities' attachment onto the graphene basal plane after oxidation. This ratio was further increased to 0.98 in FGO due to additional structural defects caused by functionalization with HMDA.[23] Moreover, the size of graphite, GO, and FGO sp^2 carbon clusters were determined according to Knight's empirical equation (Equation (1)).[24]

$$L_a = \frac{4.35}{(I_D/I_G)} \quad (1)$$

where L_a is the size of the sp^2 carbon clusters and I_D/I_G is the ratio of the intensity of the D and G bands. The data obtained (Table 1) revealed that the size of graphitic domains was decreased by functionalization with HMDA, which could be due to the gradual reduction of the graphitic structure after functionalization. Finally, the G band's position showed a gradual blueshift from 1594 to 1598 and 1609 cm^{-1} for GO and FGO, respectively, indicating a decrease in the number of graphene layers during oxidation/functionalization,[25] which scanning electron microscopy (SEM) images further confirm (see Section 2.1.5).

2.1.2. CHNS Analysis

GO functionalization with HMDA was further investigated by elemental analysis. The elemental analysis results, including carbon, hydrogen, oxygen, and nitrogen concentrations before and after graphene oxidation and functionalization, are presented in **Table 2**. According to these data, the presence of 8.2 wt% of the nitrogen in the FGO elemental analysis result confirmed that HMDA was grafted onto the surface of GO. The O/C atomic percentage was furthermore used to confirm graphite oxidation and GO reduction during functionalization. The O/C increased from 6.3% for the graphite to 84.9% for GO, confirming the oxidation of graphite and insertion of carboxylic acid, hydroxyl, and epoxy groups on the edge surface of graphite. The O/C was decreased to 37.4% for FGO, indicating that GO reduction occurred after functionalization with HMDA, as further confirmed by thermogravimetric analysis (TGA) and SEM results.

2.1.3. X-Ray Diffraction (XRD) Analysis

XRD was applied to study the changes to the structure and layer distance of prepared graphene-based materials after oxidation and functionalization with HMDA. The XRD patterns

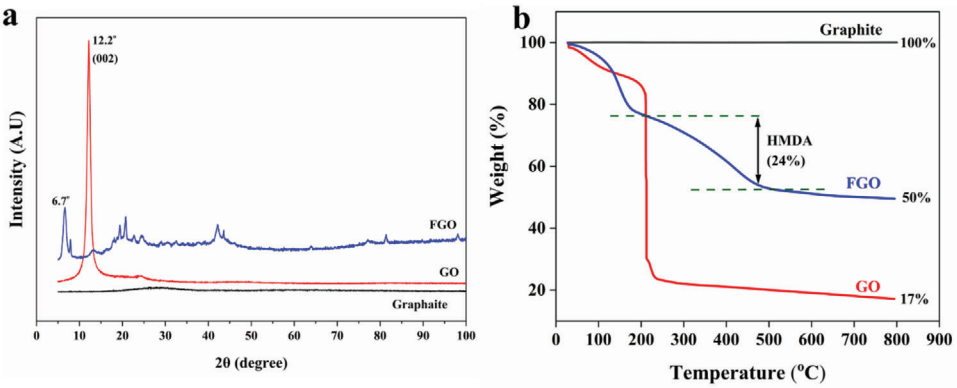

Figure 3. a) XRD patterns and b) TGA thermograms of graphite, GO, and FGO.

of graphite, GO, and FGO is presented in **Figure 3**a. Graphite showed a broad peak (002) centered at $2\theta = 28^{\circ}$ with an interplanar distance, d_{002}, of 3.21 Å. This peak was shifted to the smaller angle of $2\theta = 12.2^{\circ}$ with a layer distance of $d = 7.33$ Å in GO. This increase was due to the insertion of O-containing groups, such as epoxides, hydroxyls, and carboxylic acids, on the surface and edges of graphene layers (Figure 1a). The diffraction peak position was shifted to an even lower angle of $2\theta = 6.7^{\circ}$ for FGO, corresponding to a graphitic layer distance of 13.16 Å. This increased layer distance could be due to the attachment of HMDA onto the surface of GO. To sum up, the XRD patterns might confirm the successful synthesis of GO and functionalization of GO with HMDA and, consequently, the intercalation of HMDA molecules between the GO sheets.

2.1.4. TGA Results

The TGA technique was used as a helpful tool to determine the amount of HMDA grafted onto the surface of GO. The TGA thermograms of graphite, GO, and FGO are presented in Figure 3b. While graphite did not show any weight loss until 800 °C, GO exhibited two significant weight losses. The first one began almost immediately above 40 °C and continued until 180 °C, with almost 10% weight loss attributable to the evaporation of water adsorbed by the oxygen-containing functional groups on the GO surface. These functional groups were then decomposed in the temperature range of 180–235 °C, contributing a further 65% weight loss.[21] The weight loss of FGO was much more moderate than that of GO, especially in the temperature range of 40–235 °C, suggesting a decrease in the amount of oxygen-containing functional groups and the reduction of GO after functionalization with HMDA. Moreover, in the TGA thermogram of FGO, a new weight loss (≈24%) was observed in the temperature range of 220–500 °C, attributable to the degradation of grafted HMDA molecules, which may confirm functionalization of GO with HMDA.

2.1.5. SEM Images

The morphology, thickness, and distance between the layers in graphite, GO, and FGO were studied using SEM analysis. The SEM images of graphite, GO, and FGO at different magnifications are presented in **Figure 4**. Although all samples exhibited layered and sheet-like 2D structures, significant differences could be distinguished. The SEM image of GO showed several crumbled layers with wrinkles and folds owing to the interaction of oxygen functional groups that existed on the GO sheets. Compared with GO, FGO had fewer layers with a greater distance between the layers, which could be due to the intercalation of HMDA between GO layers, as previously observed in the XRD patterns. Furthermore, FGO presented a more extensively curled morphology, with transparent, thin, wrinkled, and paper-like structures, which could have contributed to removing the oxygen-containing functional groups from the GO surface through functionalization of GO with HMDA. Moreover, as shown, the number of layers was decreased after GO surface modification with HMDA.

2.2. Characterization of PA-FGO Nanocomposites

2.2.1. Crystallization Behavior of PA and PA-FGO Nanocomposites

The XRD patterns of PA and PA-FGO nanocomposites are presented in **Figure 5**a. All samples presented two diffraction peaks at 20° and 24°, indicating the formation of α- and γ-crystalline phases in the AABB-type PAs [26] By increasing FGO content, the intensity of the α-phase was increased, indicating that FGO acted as a nucleating agent to enhance the formation of the α-crystalline pattern. Since the α-phase is known to be more thermodynamically stable than the γ-phase,[27] it could be concluded that, compared to the PA matrix, the thermodynamic stability of the PA-FGO2 nanocomposite was significantly improved. However, at higher loading of FGO (3 wt%), the intensity of α-phase decreased, which might be due to the aggregation of FGO in the polymer matrix.

Figure 5b illustrates the differential scanning calorimetry (DSC) thermograms of the PA and PA-FGO nanocomposites during the second heating and cooling cycles. Furthermore, the relevant properties, including T_m, T_c, ΔH_m, ΔH_c, and $\chi_{c,}$ are provided in **Table 3**. Two endothermic peaks and one exothermic peak were detected in all samples, indicating that no new crystalline phases were formed after the addition of FGO. The dual endothermic peaks could suggest the melting point of the

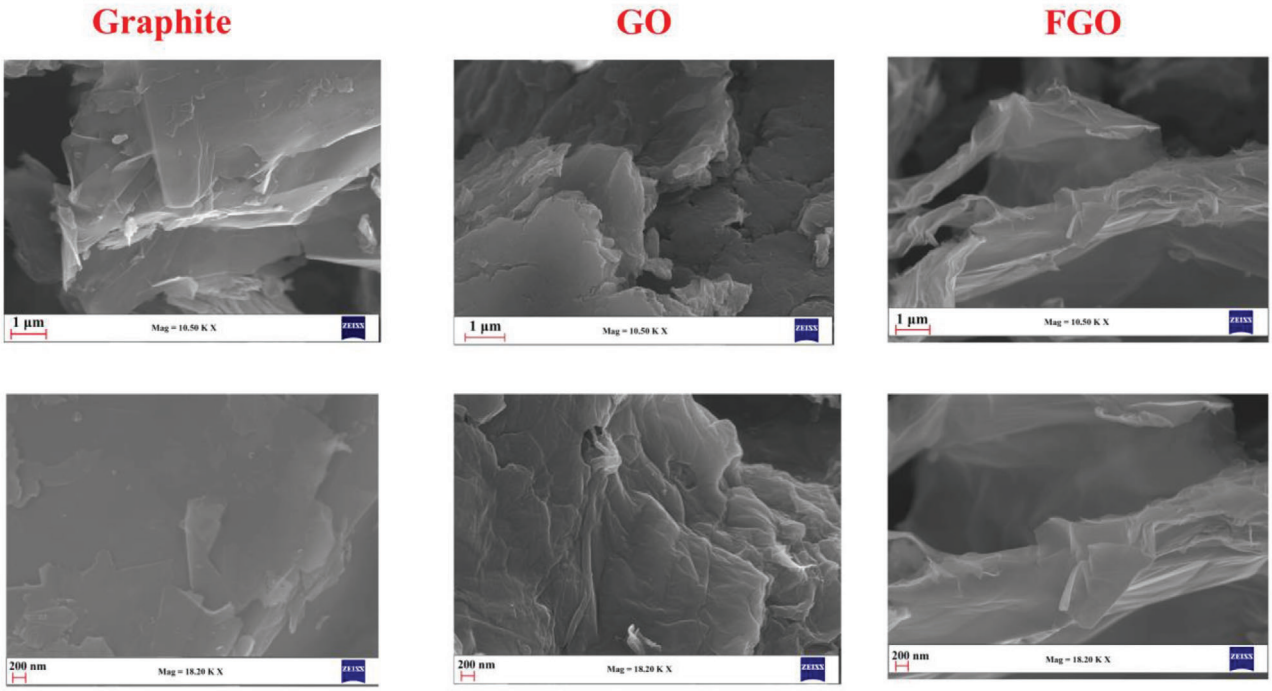

Figure 4. SEM images of graphite, GO, and FGO at different magnifications.

different crystalline forms or the melting of crystallites of the same type but different thickness.[28,29] Furthermore, the degree of crystallinity declined upon increasing the FGO content, from 27% in the PA to 18% in the PA-FGO2 nanocomposite, which could be due to the reaction between the FGO functional groups and monomers during the polymerization restricting the movement of polymer chains and hindering crystallization.[30,31] A decrease in the free volume of polymer chains caused by the presence of FGO, and a consequent restriction of movement of polymer chains that could not rearrange and form crystals comfortably, was reported as another reason for reducing crystallinity upon addition of FGO.[10,29,32] However, the degree of crystallinity increased at 3% loading of FGO, probably due to the higher free volume caused by the fillers' aggregation. Eventually, the crystallization temperature did not change remarkably over FGO loading (Figure 5c), while the crystallization enthalpy decreased significantly, indicating a slower crystallization rate in nanocomposite than in pure PA.[10,33]

2.2.2. Thermal Degradation Study

The thermal stability of the synthesized samples was investigated using TGA thermograms. **Figure 6** depicts the weight loss (TG) and derivative weight loss curves. Furthermore, the corresponding data, including temperature at 5%, 10%, and maximum weight loss ($T_{5\%}$, $T_{10\%}$, and T_{max}) and residual material (RM), are summarized in Table 3. Similar thermal degradation was observed for all samples, including good thermal stability below 400 °C and a complete decomposition between 400 and 500 °C. However, by comparing different thermal degradation temperatures, a significant improvement could be concluded for nanocomposite samples. Namely, $T_{5\%}$, $T_{10\%}$, and T_{max} were increased from 399.9, 409.0, and 435.9 °C in PA to 414.0, 426.0, and 458.5 °C in PA-FGO2 nanocomposite, respectively. The uniform dispersal of 2D FGO into the PA matrix created a tortuous path for air and prevented/hindered the removal of volatile degradation products, consequently delaying the thermo-oxidative degradation of the material.[32,34,35] On the other hand, good compatibility and better interface interactions between FGO and PA, resulting from the surface modification of GO through the grafting of HMDA chains, may delay the thermal decomposition process and improve thermal stability.[30] It is worth noting that the RM at 700 °C was enhanced by increasing the FGO loading and had good agreement with the calculated residual material (considering the residual of the pure PA and FGO at 700 °C).

2.2.3. Mechanical Properties and Electrical Conductivity

The typical stress–strain curves and mechanical properties of samples, including Young's modulus, tensile strength, elongation at break, and toughness, are provided in **Figure 7** and **Table 4**. The results revealed that incorporating FGO into the PA matrix had significantly impacted the mechanical behavior of nanocomposites. Specifically, the matrix's tensile modulus and strength exhibited 30% and 48% improvements, respectively, in the PA-FGO2 nanocomposite. It is known that the mechanical properties of polymer/graphene nanocomposites are strongly affected by the dispersion, aspect ratio, and polymer/fillers interface.[36] Accordingly, the observed improvement was assigned to the uniform dispersion of FGO into the PA matrix caused by in situ polymerization, leading to a remarkable transfer of the applied stress from the PA matrix to graphene nanoplatelets. This could

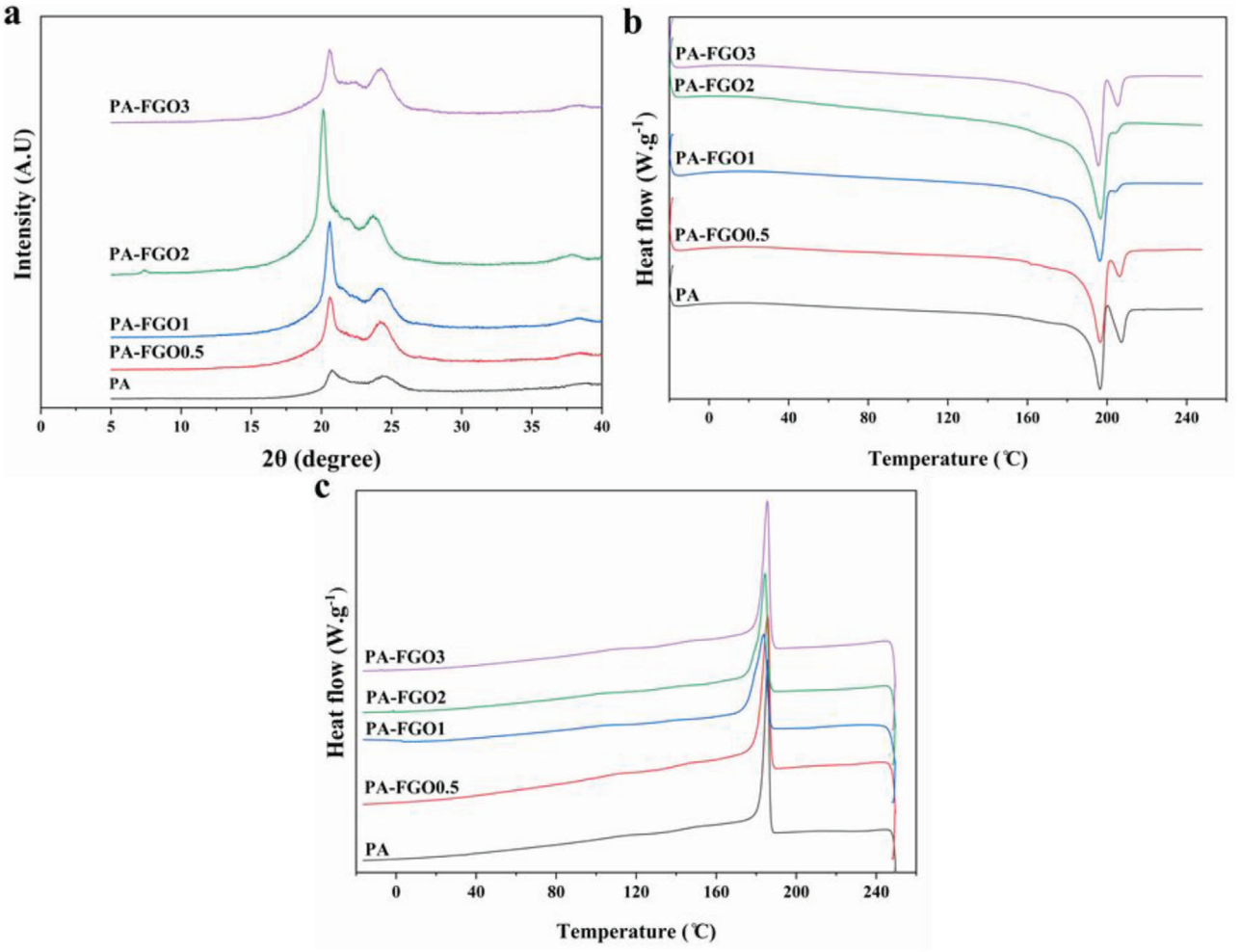

Figure 5. a) XRD patterns and b,c) DSC thermograms of PA and PA-FGO nanocomposites.

Table 3. DSC and TGA data for PA and PA-FGO nanocomposites.

Sample	T_m [°C]	ΔH_m [j g^{-1}]	χ_c, [%]	T_c [°C]	ΔH_c [j g^{-1}]	$T_{5\%}$ [°C]	$T_{10\%}$ [°C]	T_{max} [a)] [°C]	RM [%]
PA	196.5, 207.1	69.79	27.05	185.8	43.25	399.9	409.0	435.9	0.21
PAFGO0.5	196.7, 206.5	51.31	19.99	185.9	40.01	412.0	422.3	452.5	0.79
PAFGO1	196.6, 205.0	46.10	18.05	183.7	39.20	416.4	426.7	456.2	1.12
PAFGO2	196.4, 204.8	45.78	18.11	184.4	35.62	414.0	426.0	458.5	2.34
PAFGO3	195.7, 205.5	60.44	24.15	185.5	37.19	418.9	430.9	461.7	3.12

[a)] The peak of the derivative of the mass loss curve.

also be attributed to the high elastic modulus and high specific surface area of graphene nanoplatelets.[20] The surface modification of the graphene sheets with amine groups, which improved the polymer/graphene sheet interface, could provide further evidence for improving the mechanical properties of the nanocomposites. Nevertheless, the mechanical properties were reduced in the PA-FGO3 nanocomposite (Figure 7a), probably due to the aggregation of the graphene nanosheets, which formed stress concentration points within the matrix. The elongation at break illustrated a systematic reduction over FGO loading, from 230% in PA to 8% in PA-FGO3, which caused a decrease in the toughness of the matrix (the area under the force–displacement curve prior to breaking point).

Moreover, since the M_w of macromolecules is the basis of the mechanical properties of polymer materials, it was measured for PA and PA-FGO nanocomposites to compare their mechanical properties. However, due to the presence of graphene in nanocomposite samples, the M_w could not be measured with gel

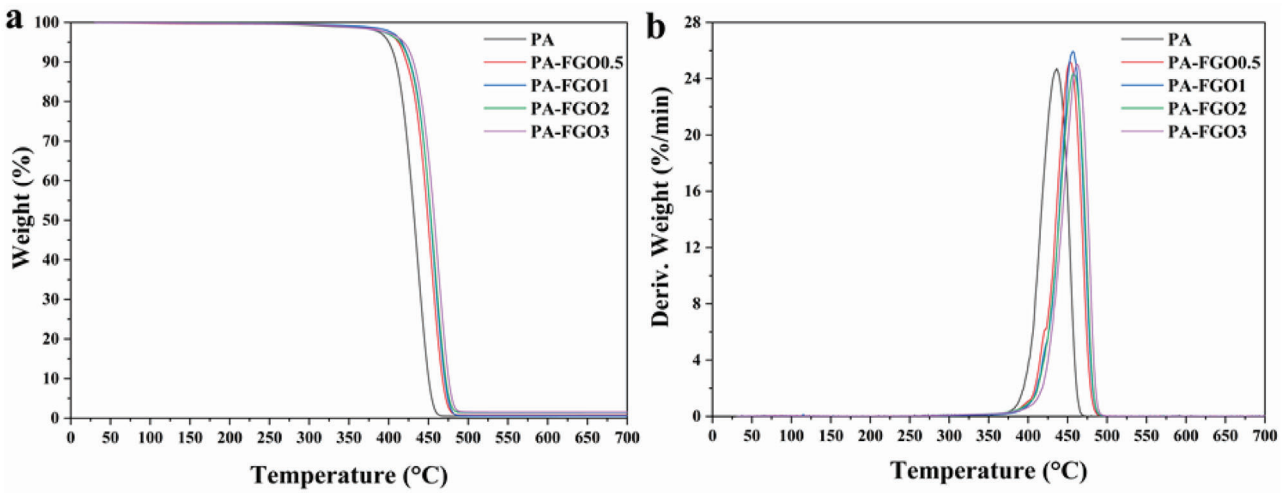

Figure 6. a) TGA and b) derivative thermogravimetric thermograms of PA and PA-FGO nanocomposites.

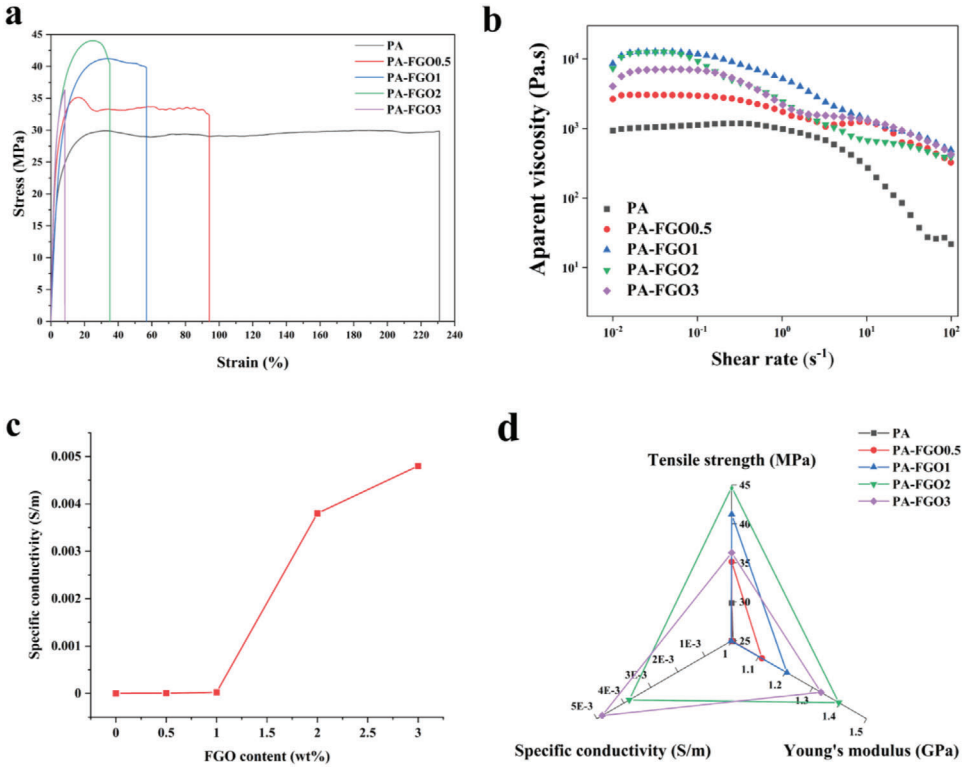

Figure 7. a) Stress–strain curves, b) apparent melt viscosity, c) specific electrical conductivity, and d) property profile of PA and PA-FGO nanocomposites.

permeation chromatography (GPC). Therefore, the melt viscosity was selected to measure the M_w of the samples. The melt viscosity when the chains start to entangle with one another is related to the M_w according to a power-law equation (Equation (5)). Figure 7b presents the apparent melt viscosity of the samples. Accordingly, the M_w of the nanocomposite samples, including PA-FGO0.5, PA-FGO1, PA-FGO2, and PA-FGO3, were calculated as 10 100, 1150, 13 500, and 10 900 g mol^{-1}. The M_w significantly increased in the nanocomposite samples by increasing the FGO content up to 2 wt%, which led to improved mechanical properties, as reported in the literature.[37]

The electrical conductivity of the prepared samples is presented in Figure 7c and Table 4. As shown, this was enhanced up to 4.8×10^{-3} S m^{-1} for PA-FGO3 by increasing the FGO content (Figure 7c and Table 4). Specifically, the incorporation of 2 wt% FGO resulted in a remarkable increase in conductivity, which may be due to the formation of conductive networks by FGO. According to Figure 7c, the content of FGO at the percolation

Table 4. The mechanical properties of the PA and PA-FGO nanocomposites.

Sample	Young's modulus [MPa]	Tensile strength [MPa]	Elongation at break [%]	Toughness [kJ m^{-2}]	M_w [g mol^{-1}]	Specific conductivity [S m^{-1}]
PA	1005 ± 35	29.82 ± 1.22	230.91 ± 10.39	27.44 ± 1.09	7200	o.r.[a)]
PA-FGO0.5	1112 ± 41	35.14 ± 1.41	94.41 ± 3.58	16.32 ± 0.63	10 100	3.60×10^{-6}
PA-FGO1	1205 ± 47	41.23 ± 1.84	56.79 ± 2.55	12.55 ± 0.51	1150	2.50×10^{-5}
PA-FGO2	1307 ± 53	44.72 ± 1.56	33.05 ± 1.23	10.99 ± 0.40	13 500	3.80×10^{-3}
PA-FGO3	1331 ± 49	36.30 ± 1.45	8.32 ± 0.36	1.84 ± 0.06	10 900	4.80×10^{-3}

[a)] o.r. indicates that the electrical conductivity was found to be out of the measurable range.

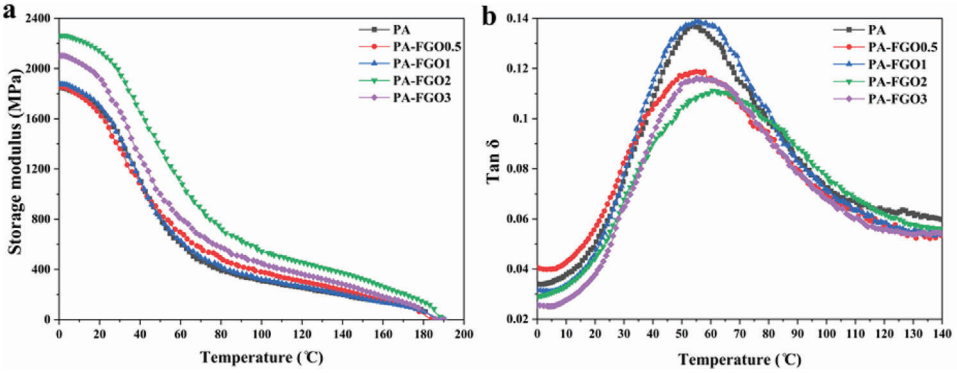

Figure 8. a) Storage modulus and b) tan δ curves of PA and PA-FGO nanocomposites versus temperature.

threshold point was about 2 wt%, which might be due to the tunneling effects that occurred between adjacent FGO nanosheets, leading to an increase in the conductivity. Moreover, the high-temperature reaction condition (230 °C) for PA-FGO nanocomposite preparation, and the hot-pressure method employed to prepare the films (220 °C and 150 kPa), may lead to FGO thermolysis reduction. At these conditions, oxygen-containing functional groups can be eliminated from the surface of FGO according to the TGA curve in Figure 3b, leading to an increase in the conductivity of FGO. Previously, Hofmann et al.[16] showed that by adding 5 wt% thermally reduced graphite oxide, the conductivity of PA12 reached 4.0×10^{-3} S m^{-1}, while in the present study, the conductivity of PA reached 3.80×10^{-3} S m^{-1} by adding only 2 wt% FGO. This phenomenon may be due to the surface functionalization of GO, the high-temperature fabrication method, and the good interfacial interactions between FGO and PA aiming at in situ polymerization.

2.2.4. Dynamic Mechanical Properties

The samples' mechanical properties in the dynamic mode were studied with dynamic mechanical analysis (DMA). **Figure 8** demonstrates the trend of storage modulus (E') and tan δ curve, which is the ratio of loss modulus (E'') over storage modulus (E'), versus temperature. On one side, E' was remarkably higher in nanocomposites than the PA matrix, particularly at lower temperatures. For instance, at 25 °C, it was 1590 and 2066 MPa for PA and PA-FGO2 nanocomposite, respectively, indicating a 30% improvement just by adding 2 wt% FGO. This enhancement is believed to be associated with the fine dispersion of FGO within the PA matrix and excellent compatibility between graphene nanosheets and polymer chains arising from successful surface modification of GO.[1,36] Nevertheless, E' dropped in PA-FGO3 nanocomposite, probably due to aggregation of GO sheets within the PA matrix, which agrees with the results observed in XRD, DSC, and mechanical tests.

On the other hand, the storage modulus reduced with increasing temperature; a mild reduction was observed below 55 °C, attributable to the increase in the segmental PA motion with temperature, followed by a sharp drop between 55 to 100 °C, corresponding to the glass transition temperature (T_g). In support of the latter, the tan δ curves (Figure 8b) of all the samples showed a peak at about 55 °C, attributable to relaxations of the polymer related to the T_g. The peak shifted to a higher temperature in the nanocomposite samples, indicating that the presence of the FGO hindered the movement of the PA chains. It could also be due to the interactions between PA and surface modified FGO, which reduced the nanocomposite system's molecular dynamics and increased the T_g.[36] However, T_g decreased in the PA-FGO3 nanocomposite, which might be due to the aggregation of FGO at higher filler content, which led to enhancing the free volume and decreasing the T_g.

2.2.5. Rheology Test

The rheological characterization was performed to further investigate the dispersion of FGO within the PA matrix. **Figure 9** demonstrates the plot of complex viscosity ($|\eta^*|$), storage

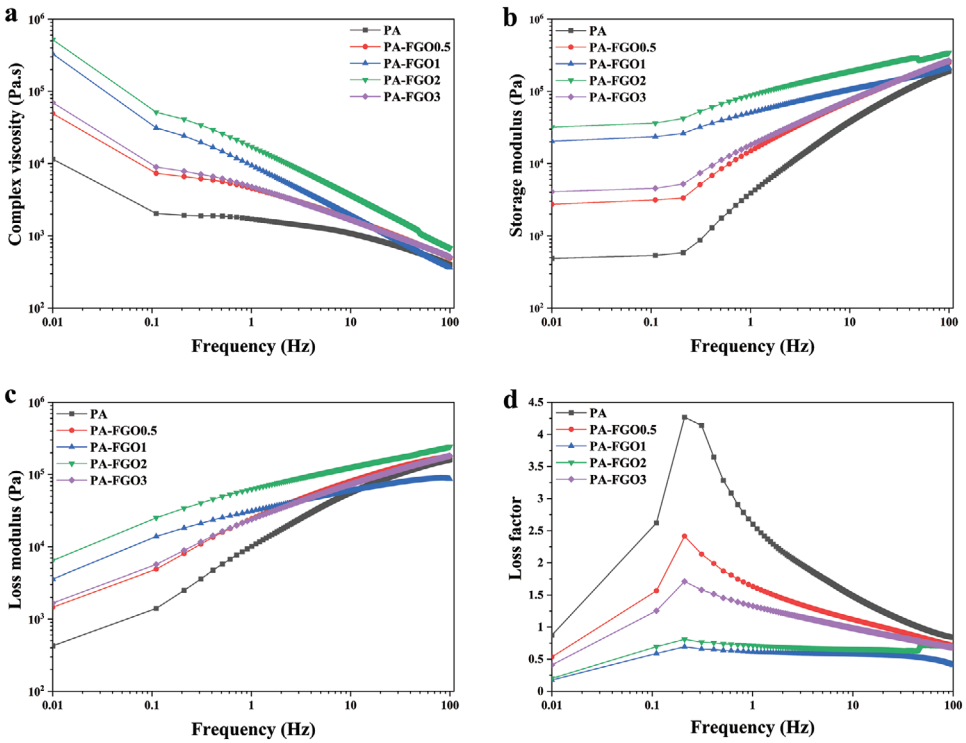

Figure 9. a) Complex viscosity, b) storage modulus, c) loss modulus, and d) loss factor curves of PA and PA-FGO nanocomposites versus frequency at 220 °C.

modulus (G'), loss modulus (G''), and loss factor of PA and PA-FGO nanocomposite versus frequency. On the one hand, the viscosity of all the samples revealed a non-Newtonian trend in which it decreased with the increase in the frequency. This trend, known as shear-thinning behavior, was attributed to the lack of time for the polymer chains to respond to the applied oscillation. Furthermore, the viscosity increased upon increasing the FGO content, contributing to the uniform dispersion of nanofillers into the matrix, and the strong Van der Waals bond interactions between FGO and PA obtained by successful surface modification of GO. Surprisingly, at higher filler loading, the viscosity dropped owing either to the alignment of the graphene platelets helping the flow in the molten state or to the plasticizing effect of the HMDA used in the FGO preparation.[38,39]

On the other hand, both G' and G'' moduli increased upon increasing the FGO loading, particularly at lower frequencies, due to the entrapment of polymer chains within the graphene sheets, forming the rigid networks, as well as the strong polymer-filler interactions.[29,36] The reduction of moduli in the PA-FGO3 sample further demonstrated the aggregation of the FGO nanoparticles at higher loading, as previously observed in the tensile test and DMA results. It is worth noting that the PA chains were fully relaxed under the rheology test conditions and exhibited a liquid-like or typical terminal behavior in which $G' < G''$ or loss factor > 1[40] (Figure 9d). Nevertheless, specific nanocomposite samples (PA-FGO1 and PA-FGO2) demonstrated solid-like behavior over frequencies in which $G' > G''$ or loss factor < 1 (Figure 9d), owing to the formation of a rigid network, as well as the strong polymer-filler interaction which caused the matrix to exhibit elastic behavior.[29,36]

2.2.6. SEM and TEM Images

The dispersion and compatibility of graphene nanosheets have key roles in determining the final properties of the nanocomposite and, therefore, its potential for engineering applications. Hence, SEM and transmission electron microscopy (TEM) techniques were used to confirm the effect of surface functionalization of GO on its dispersion in the polymer matrix and its compatibility with PA. The combination of the comprehensive evaluations of the mechanical properties and conductivity of nanocomposites (Figure 7d) and their thermal and rheological results revealed that the nanocomposite containing 2% of FGO had better performance than the others. Therefore, the PA-FGO2 nanocomposite was selected for SEM and TEM imaging. **Figure 10**a,b presents the SEM cross-section images of pure PA and PA-FGO2 nanocomposite at different magnifications. The FGO sheets with a uniformly narrow thickness, folded, and with bright edges were dispersed homogeneously in the polymer matrix, indicating the benefit of employing in situ polymerization, in which the monomers reacted in between the graphene layers. Furthermore, no evidence of aggregation and formation of any voids could be detected around the FGO sheets, confirming the enhanced interfacial interactions of graphene layers with the PA matrix and excellent compatibility between two phases resulting from HMDA grafting on the GO surface. Moreover, TEM images of PA-FGO2 (Figure 10c) revealed that the FGO nanosheets were thoroughly exfoliated and well-dispersed in the PA matrix. It was observed that the surface of graphene nanosheets was wrinkled, which was due to surface modification with HMDA and interfacial interactions with PA chains.

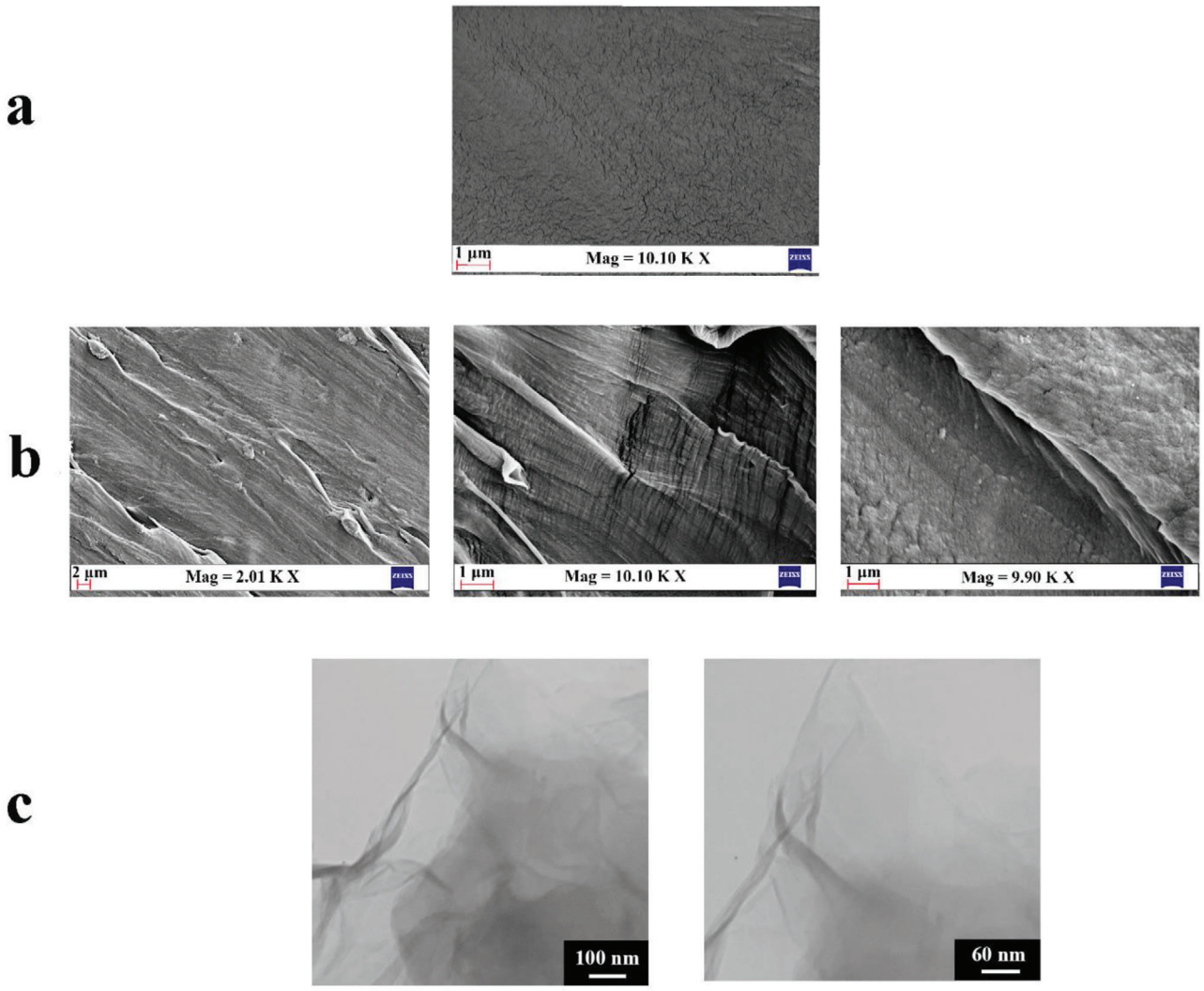

Figure 10. SEM cross-section images of a) PA and b) PA-FGO2 nanocomposite at different magnifications. (c) TEM images of PA-FGO2 nanocomposite at different magnifications.

3. Conclusion

A series of biobased long-chain aliphatic PA/FGO was successfully developed via in situ polymerization. The surface of GO was functionalized with HMDA molecules to graft free amine groups for in situ polymerization with diacid. Consequently, the compatibility and interactions between polymer and filler phases were improved. The FT-IR, Raman, elemental analysis, XRD, and TGA results, as well as SEM images, confirmed the successful surface modification of GO sheets. By adding only 2 wt% of FGO, the mechanical properties of PA were improved remarkably in static and dynamic modes. A similar improvement was also observed in the thermal stability of the nanocomposite. Furthermore, the rheology test results revealed a significant increase in the storage modulus of the matrix upon increasing the FGO content. The electrical conductivity of the nanocomposites was also enhanced by increasing the FGO content and the incorporation of 2 wt% FGO resulted in a remarkable increase in conductivity, which may be due to the formation of conductive networks by FGO. These improved properties were all attributed to the excellent compatibility of PA and FGO owing to the surface modification of GO with HMDA and using in situ polymerization. Altogether, the finding of this study confirmed the outstanding thermomechanical properties of the newly developed biobased PA-FGO nanocomposites, which could provide exciting alternatives to the common petroleum-based thermoplastic for demanding engineering applications.

4. Experimental Section

Materials: 1,14-Tetradecanedioic acid (TDA) was provided by Zibo Guangtong Chemical Company, China. Graphite powder with particle size less than 20 μm, HMDA, sulfuric acid (H_2SO_4 98%), hydrochloric acid (HCl), potassium permanganate ($KMnO_4$), sodium hypophosphite monohydrate (≥99%), hydrogen peroxide (H_2O_2), and dimethyl sulfoxide were purchased from Sigma-Aldrich, UK. Ethanol (92.4%, ETAX B) was provided from ALTIA Industrial, Finland.

Graphene Oxide Preparation and Functionalization: Hummer's method, with significant modifications, was employed to prepare

graphene oxide.[41] Graphite powder (2.5 g) was added to a mixture of concentrated H_2SO_4 (60 mL) and $NaNO_3$ (1.25 g) at 0 °C. $KMNO_4$ (7.5 g) was then added gradually while the system was stirred at a temperature below 20 °C. Then, the mixture was stirred at 35 °C for 30 min. 125 mL of distilled water was then added and the mixture was stirred at 98 °C for a further 1 h. The reaction was terminated by adding 350 mL of distilled water and then 10 mL of H_2O_2 (30%). The color change to brilliant yellow after adding H_2O_2 confirmed the oxidation of graphite and that graphite oxide had been obtained. Graphite oxide was separated by centrifuging the mixture at 4000 rpm for 5 min and then washed with distilled water and 10% HCl solution to remove the residual metal ions. The synthesized graphite oxide was sonicated for 1 h to convert into exfoliated GO, centrifuged, and dried for 24 h.

The dried GO (2.5 g) was dispersed in dimethylformamide (500 mL), using ultrasonication to obtain a homogeneous suspension. After this, HMDA (25 g) was added into the mixture, and the system was stirred continuously overnight at 60 °C under nitrogen gas flow. The mixture was then centrifuged at 4000 rpm for 10 min, washed several times with ethanol, and freeze-dried for 48 h. The functionalized GO powder was named FGO and used as a nanofiller to prepare PA-FGO nanocomposites through in situ polymerization.

Synthesis of PA614 and PA-FGO Nanocomposites: PA614 was synthesized according to the previous work.[3] Equal moles of TDA and HMDA were added to a reactor equipped with an overhead stirrer, heating jacket, and nitrogen flow. 0.1% of the weight of the monomers, sodium hypophosphite monohydrate was added as a catalyst. At first, the temperature was set to 140 °C for 1 h in order to melt the monomers, and then, the reaction was continued at 230 °C for 8 h under nitrogen flow. Finally, the reactor was cooled while it was kept under nitrogen to avoid any oxidation. The resulting polymer was milled using a Retsch SM 300 Cutting Mill with a blade size of 1 mm at 1000 round per minute and then hot-pressed at 220 °C to prepare the film.

In situ polymerization was employed for the synthesis of PA-FGO nanocomposites. Initially, FGO was dispersed in ethanol by sonication for 60 min, then TDA was added, and the mixture was stirred for 4 h. The TDA/FGO mixture was dried at room temperature overnight and fed into the reactor with HMDA and catalyst. The rest of the polymerization was similar to the method previously described for the pure PA. The molar ratio between the carboxylic groups (from TDA) and the amine groups (from HMDA and FGO) was kept at 1. The amounts of FGO in the PA matrix were 0.5, 1, 2, and 3 wt%, and the corresponding synthesized nanocomposites were coded as PA-FGO0.5, PA-FGO1, PA-FGO2, and PA-FGO3, respectively.

Characterization: *FT-IR*: FT-IR analysis was performed in the range 500–4000 cm^{-1} using a PerkinElmer FT-IR spectrometer with attenuated total reflectance at a resolution and scan number of 4 cm^{-1} and 32, respectively.

Raman Spectroscopy: Raman spectroscopy measurements were carried out using LabRAM HR UV-NIR and PARK XE-100 atomic force microscopy instruments at a wavelength of 514 nm from 500 to 3500 cm^{-1} using an Ar laser source.

Elemental Analysis: Elemental analysis was performed with FlashSmart EA carbon, hydrogen, nitrogen, sulfur, and oxygen (CHNS/O) instrument manufactured by Thermo Scientific, USA, to confirm the functionalization degree of GO with HMDA.

XRD: The interlayer distance between the GO layers, and the crystallinity behavior of the PA and PA-FGO nanocomposites, were investigated by PANalytical X'Pert Powder XRD (alpha-1) at an X-ray wavelength of 1.54 Å, and a voltage and current of 45 kV and 40 mA, respectively. Bragg's equation was used to calculate the d-spacing of the graphene sheets (Equation (2)).

$$n\lambda = 2d\sin(\theta) \tag{2}$$

where n is the order of refraction, λ is the wavelength of the X-rays (1.54 Å), and θ is the angle of incidence.

SEM: The morphology of the synthesized GO, FGO, and the cross-sectional area of the cryofracture PA and PA-FGO nanocomposite were observed under high vacuum using a scanning electron microscope (SEM, Zeiss Sigma VP) at a voltage of 10 kV. All the samples were gold/palladium sputtered (4 nm) before imaging.

Electrical Conductivity: The four-point probe technique (Jandel Engineering Ltd., Jandel RM3000) was employed to measure the electrical conductivity of the samples using Equation (3), where σ is conductivity (S m^{-1}), and ρ is specific resistivity. ρ was calculated through Equation (4), in which R_s is sheet resistance (Ω sq^{-1}), and t is the thickness of the sample (m).

$$\sigma = 1/\rho \tag{3}$$

$$\rho = R_s \times t \tag{4}$$

Mechanical Properties: The mechanical properties of the dog bone-shaped specimens were investigated using an Instron 5944 universal tensile testing machine. The load was fixed at 2 kN and the tensile rate at 5 mm min^{-1}. Each measurement was repeated three times and averaged. Moreover, the dynamic mechanical properties of the thin strip-shaped specimens were measured using a TA Instruments Model Q800 from 25 to 200 °C at a heating rate of 5 °C min^{-1}. The frequency, strain rate, and preload were fixed at 1 Hz, 0.5%, and 1 N, respectively. The storage modulus (E'), loss modulus (E''), and tan δ versus temperature curves were extracted and studied.

Molecular Weight (M_w): The M_w of pure PA614 was measured with the GPC) using the Water 717 Plus Autosampler device, equipped with two Agilent 5 µm mixed bed columns. Chloroform with 10% v/v trifluoroacetic anhydride was used as a solvent and applied at a flow rate of 1.0 mL min^{-1}. The sample concentration was ≈1 mg mL^{-1}. Narrow molar mass distribution polystyrene standards were used for the calibration of the columns. The melt viscosity was also applied to measure the M_w of the PA-FGO nanocomposite samples using a power-law equation[42] (Equation (5)):

$$\eta_0 = kM_W^n \tag{5}$$

where η_0 is a zero shear-rate viscosity and n is the power-law coefficient with a value of about 3.4 ± 0.2. The obtained M_w of the pure PA through GPC (M_w = 7200 g mol^{-1}) was used to calculate the k value.

DSC: The crystallization behavior and melting point of the samples were investigated using an MT-DSC Q2000 analyzer equipped with an intercooler. Two heating-cooling cycles were used between −20 and 250 °C with a rate of 10 °C min^{-1} under a nitrogen atmosphere. The first cycle was used to erase the thermal history of the polymer and the second one was employed to determine the crystallization temperature (T_c), melting temperature (T_m), crystallization enthalpy (ΔH_c), and melting enthalpy (ΔH_m) of the samples. The degree of crystallinity (χ_c) was calculated using Equation (6).

$$\chi_c = \frac{\Delta H_m}{\Delta H_m^0 (1 - x_f)} \times 100 \tag{6}$$

where ΔH_m^0 is the melting enthalpy of a 100% crystalline specimen and x_f is the filler weight fraction in the nanocomposite. The value of purely crystalline PA612 (258 J g^{-1}) was used as the melting enthalpy of 100% crystalline PA614 because it is the closest structural counterpart to PA614.[5,28]

TGA: The samples' thermal degradation was investigated by TGA using a TA instruments Q500. The sample was heated from 30 to 700 °C, with a heating rate of 10 °C min^{-1} under a nitrogen atmosphere.

Rheology: The viscoelastic performance of the molten samples was studied using an Anton Paar Physica MCR 301 rotational rheometer at a constant strain of 1%. The samples were first molten at 220 °C; the trend of storage modulus (G'), loss modulus (G''), and the complex viscosity ($|\eta^*|$) versus frequency was then monitored between 0.01 and 100 Hz. The apparent melt viscosity versus share rate trend within 0.01–1000 s^{-1} was measured at 220 °C and used to calculate the nanocomposite molecular weight through Equation (5).

Acknowledgements

H.B. and S.B. contributed equally to this work. The authors would like to acknowledge the Academy of Finland funding, Nos. 327248 (ValueBiomat) and 327865 (Bioeconomy).

Conflict of Interest

The authors declare no conflict of interest.

Data Availability Statement

Data sharing is not applicable to this article as no new data were created or analyzed in this study.

Keywords

biobased polyamide, functionalized graphene oxide, in situ polymerization, nanocomposites

Received: April 14, 2021
Revised: May 19, 2021
Published online:

[1] F. C. Chiu, I. N. Huang, *Polym. Test.* **2012**, *31*, 953.
[2] R. Ajdary, N. Kretzschmar, H. Baniasadi, J. Trifol, J. V. Seppälä, J. Partanen, O. J. Rojas, *ACS Sustainable Chem. Eng.* **2021**, *9*, 2727.
[3] H. Baniasadi, J. Seppälä, *Mater. Today Chem.* **2021**, *20*, 1.
[4] S. P. Rwei, P. Ranganathan, Y.-H. Lee, *J. Mol. Struct.* **2019**, *1186*, 285.
[5] P. H. Nguyen, S. Spoljaric, J. Seppälä, *Polymer (Guildford, Engl.)* **2018**, *153*, 183.
[6] L. Duarte, S. Nag, M. Castro, E. Zaborova, M. Ménand, M. Sollogoub, V. Bennevault, J. F. Feller, P. Guégan, *Macromol. Chem. Phys.* **2016**, *217*, 1620.
[7] P. Radzik, A. Leszczyńska, K. Pielichowski, *Polym. Bull.* **2020**, *77*, 501.
[8] J. H. Wu, C. W. Chen, M. C. Kuo, M. S. Yen, K.-Y. Lee, *J. Polym. Environ.* **2018**, *26*, 626.
[9] H. Baniasadi, J. Trifol, A. Ranta, J. Seppälä, *Composites, Part B 211*, **2021**, 108655.
[10] M. Adel, O. El-Shazly, E.l-W. F. El-Wahidy, A. El-Maghraby, M. A. A. Mohamed, *Polym. Eng. Sci.* **2018**, *58*, 1201.
[11] J. Minář, J. Brožek, A. Michalcová, R. Hadravová, P. Slepička, *Composites, Part B* **2019**, *174*, 1.
[12] A. Inurria, P. Cay-Durgun, D. Rice, H. Zhang, D. K. Seo, M. L. Lind, F. Perreault, *Desalination* **2019**, *451*, 139.
[13] H. V. Madhad, D. V. Vasava, *J. Thermoplast. Compos. Mater.* **2019**, https://doi.org/10.1177/0892705719880942.
[14] J. Li, W. Zhu, S. Zhang, Q. Gao, J. Li, W. Zhang, *Polym. Test.* **2019**, *76*, 232.
[15] M. Fathizadeh, H. N. Tien, K. Khivantsev, Z. Song, F. Zhou, M. Yu, *Desalination* **2019**, *451*, 125.
[16] D. Hofmann, M. Keinath, R. Thomann, R. Mülhaupt, *Macromol. Mater. Eng.* **2014**, *299*, 1329.
[17] Y. H. Yang, L. Bolling, M. A. Priolo, J. C. Grunlan, *Adv. Mater.* **2013**, *25*, 503.
[18] F. J. Tölle, M. Fabritius, R. Mülhaupt, *Adv. Funct. Mater.* **2012**, *22*, 1136.
[19] H. Kim, A. A. Abdala, C. W. Macosko, *Macromolecules* **2010**, *43*, 6515.
[20] A. E. M. Hassan, A. I. Eid, M. El-Sheikh, W. Y. Ali, *Materwiss. Werkstttech.* **2019**, *50*, 74.
[21] S. Mallakpour, A. Abdolmaleki, S. Borandeh, *Appl. Surf. Sci.* **2014**, *307*, 533.
[22] S. Gurunathan, J. Han, J. H. Kim, *Colloids Surf., B* **2013**, *111*, 376.
[23] A. Abdolmaleki, S. Mallakpour, S. Borandeh, *Polym. Compos.* **2016**, *37*, 1924.
[24] D. S. Knight, W. B. White, *J. Mater. Res.* **1989**, *4*, 385.
[25] S. Borandeh, A. Abdolmaleki, S. S. Abolmaali, A. M. Tamaddon, *Carbohydr. Polym.* **2018**, *201*, 151.
[26] L. Jasinska, M. Villani, J. Wu, D. Van Es, E. Klop, S. Rastogi, C. E. Koning, *Macromolecules* **2011**, *44*, 3458.
[27] N. Mahmood, M. Islam, A. Hameed, S. Saeed, *Polym.* **2013**, *5*, 1380.
[28] P. H. Nguyen, S. Spoljaric, J. Seppälä, *Eur. Polym. J.* **2018**, *109*, 16.
[29] R. Scaffaro, A. Maio, *Composites, Part B* **2019**, *165*, 55.
[30] Y.-Z. Wang, X. F. Gao, H. H. Liu, J. Zhang, X. X. Zhang, *Mater. Chem. Phys.* **2020**, *240*, 122288.
[31] H. Liu, L. Hou, W. Peng, Q. Zhang, X. Zhang, *J. Mater. Sci.* **2012**, *47*, 8052.
[32] D. Zhu, Y. Ren, G. Liao, S. Jiang, F. Liu, J. Guo, G. Xu, *J. Appl. Polym. Sci.* **2017**, *134*, 1.
[33] C. C. N. De Melo, C. A. G. Beatrice, L. A. Pessan, A. D. De Oliveira, F. M. Machado, *Thermochim. Acta* **2018**, *667*, 111.
[34] Y. Zhang, Y. Lu, X. Yan, W. Gao, H. Chen, Q. Chen, Y. Bai, *Composites, Part A* **2019**, *123*, 149.
[35] A. Dorigato, A. Pegoretti, *Polym. Eng. Sci.* **2019**, *59*, 198.
[36] B. J. Rashmi, K. Prashantha, M.-F. Lacrampe, P. Krawczak, *Adv. Polym. Technol.* **2018**, *37*, 1067.
[37] T. D. Fornes, P. J. Yoon, H. Keskkula, D. R. Paul, *Polymer (Guildford, Engl.)* **2001**, *42*, 09929.
[38] M. Abdelwahab, A. Codou, A. Anstey, A. K. Mohanty, M. Misra, *Composites, Part A* **2020**, *129*, 105695.
[39] M. E. M. Mekhzoum, M. Raji, D. Rodrigue, A. el kacem Qaiss, R. Bouhfid, *Appl. Clay Sci.* **2020**, *185*, 1.
[40] L. Shen, Y. Lin, Q. Du, W. Zhong, Y. Yang, *Polymer (Guildford, Engl.)* **2005**, *46*, 5758.
[41] W. S. Hummers, R. E. Offeman, *J. Am. Chem. Soc.* **1958**, *80*, 1339.
[42] P. R. Lewis, *Forensic Polymer Engineering: Why Polymer Products Fail in Service*, 2nd ed., Woodhead Publishing, Sawston, UK **2016**.